

# Online Measurement of the GMAW Process Using Composite Sensor Technology

*A monitoring system with active and passive vision has been developed for the online measurement of weld bead and weld pool geometry*

BY Z. JIN, H. LI, Q. WANG, AND H. GAO

## ABSTRACT

Controlling the geometric parameters of the weld pool and the weld bead is the main method for getting better welding quality in industrial robotic welding. This paper presents the technology on a real-time welding process sensor, which is necessary to improve welding quality using an intelligent robot during the gas metal arc welding process. A set of vision systems, which consists of an active vision sensor and a passive vision sensor, has been designed. The clear, steady images of the weld pool were obtained by the passive vision part, and the images of the laser stripe projected on the weld bead were obtained by the active vision part, at the same time. The features of the acquired images were analyzed, and the geometric parameters of the weld cross section and the weld pool were successfully extracted from the images. The detection precision of the system was also analyzed.

## KEYWORDS

- GMAW • Weld Pool and Weld Bead Geometry • Composite Sensor Technology
- Image Processing • Least Square Method

## Introduction

Among the various welding processes that have been developed so far, gas metal arc welding (GMAW) is one of the most successfully and widely used methods (Ref. 1). Because of its high productivity, reliability, and easy automation, GMAW is also considered to be a favorable welding method for robotic applications (Ref. 2). However, sheet and bottom welds are a challenge in robotic GMAW because the process tends to produce melt-through or incomplete penetration. Thus, an intelligent GMAW robotic system is urgently needed.

Welding quality control and joint tracking technology are two fundamental topics in automated robotic welding (Ref. 3). A perfect solution for joint tracking and quality control is the precondition of realizing welding automation, and that welding quality control is the major difficulty. In the process of actual welding, the weld pool and the weld bead always contain a wealth of useful information, which tends to reflect weld penetration and

other factors related to weld quality (Ref. 4).

To date, the main sensing methods for weld quality control include ultrasonic sensing (Ref. 5), infrared sensing (Ref. 6), x-ray sensing (Ref. 7), and vision sensing (Refs. 8–14). Vision sensing has better application prospects because its function is much more similar to the eyes of the human welder, and it can also provide more information on the welding process than other sensing methods.

However, most of the research mainly focuses on GTAW, as it is more stable during the welding process and easier to get a clear weld pool image. In Refs. 15–17, the researchers characterized the three-dimensional (3D) weld pool surface by using 3D vision sensing technology. This technology showed the weld pool surface as a mirror. A laser pattern was projected onto the specular surface of the weld pool, and its reflection from the specular surface was intercepted. Reflection law was used to compute the

weld pool surface, which determines the reflection of the projected laser pattern.

However, the weld pool surface, especially the GMAW pool surface, is always unstable because of dynamic vibration and molten slags, which cause the reflected laser lines to be mixed and disordered. In this case, the reconstruction of the 3D weld pool surface using this method will be difficult.

Aviles-Vinas et al. (Refs. 18, 19) used a laser-based sensor to measure the bead geometry (width and height) for the input signal of the control system. The red line pattern from the laser generator was projected onto the weld bead, and a camera was used to capture the image of the laser line on the weld bead. An artificial neural network (ANN) based architecture was proposed to learn welding skills automatically. The laser beam was 5 cm apart from the welding torch to avoid excessive light, which would have introduced a 5 to 12.5 s delay (as the welding speed is used between 4 to 10 mm/s) to the control system.

Because the geometry features of the weld pool and weld bead reflect the quality of the welding process, this paper develops a monitoring system comprised of an active vision sensor and a passive vision sensor for online measurement of the weld bead and weld pool geometry. A series of image processing algorithms are developed and verified through the comparison between the manual measurement and the sensing detection. The research provides a powerful sensing method for multivariable control of the GMAW process for sheet and bottom welds. Our future work will concentrate on the design of the control system itself.

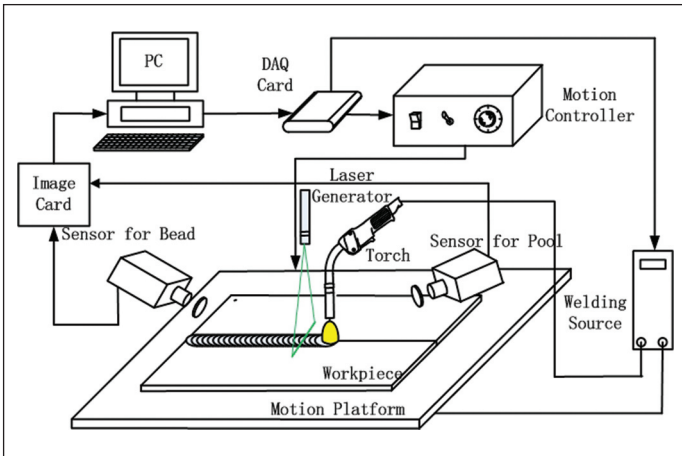


Fig. 1 — Schematic diagram of the experimental system.

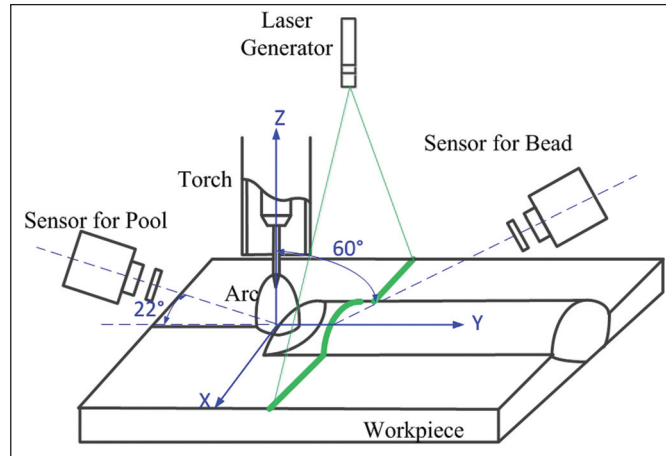


Fig. 2 — Active-passive composite vision sensing system design.

## Experimental System Design

The experimental system setup is illustrated in Fig. 1. It consisted of four parts: GMAW system, moving system, monitoring system including active and passive vision parts, and industry personal computer, which was the core of the system. The moving system was controlled by the industry personal computer through the data acquisition (DAQ) card and the motion controller. The welding system was also controlled by the industry personal computer through the DAQ card. During the GMAW process, the welding torch was fixed on a stationary, thick plate.

The vision-based sensing system was the basis for the online measurement of the weld pool and weld bead geometry. As shown in Fig. 2, the vision-based sensing system consisted of an active vision sensor and a passive vision sensor. The active vision sensor was used for weld bead geometry measurement. It was composed of a charge-coupled device (CCD) camera with 60 fps, a laser generator, and a narrow band filter. The angle between the camera and the torch was about 60 deg. In the active vision sensor system, the 530-nm laser with 200-mW power output was chosen because the red laser stripe would be buried in the radiation light from the high-temperature metal behind the pool. The distance between the laser stripe and the torch was about 2.2 cm, which is much smaller than the system in Refs. 18 and 19 — Fig. 3. In other words, the

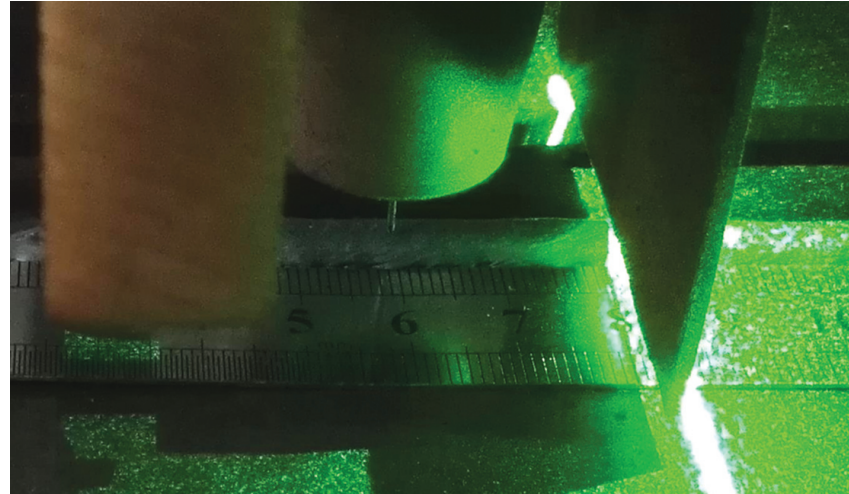


Fig. 3 — The relative location between the laser stripe and the weld wire.

delay of our system was much smaller than the system in Refs. 18 and 19.

The passive vision sensor was used for the pool geometry measurement. It was composed of a CCD camera with 60 fps and a narrow band filter. When detecting from the rear of the torch, the light intensity of the pool tail was a little weaker than the radiation light of the high-temperature metal behind the pool, and the gray scale difference was smaller than 5, which makes the pool tail almost impossible to be extracted. Since the weld pool is just like a mirror that reflects the strong arc light projected on it, the light intensity of the pool tail was fainter than the high-temperature metal behind the pool when detecting from the front of the torch. The angle between the camera and the torch was about 68 deg. The central wavelength of the filter was 650 nm, which is chosen accord-

ing to the characteristic of the GMAW arc spectrum of steel. The intensity in the wavelength range from 600 to 700 nm was relatively weak. The image software of the two cameras mentioned in our paper was developed by us, so the synchronization acquisition of the two cameras was performed by using our own image acquisition software.

The reason for this design was as follows. The weld penetration state was really tough to be estimated just through the 2D geometry of the pool. The change of the weld penetration state is a continuous gradual process; namely, the current weld penetration state was closely bound up with the previous weld penetration states. The previous weld penetration states can be estimated through the weld bead geometry, so the weld bead geometry can be used to predict the current weld

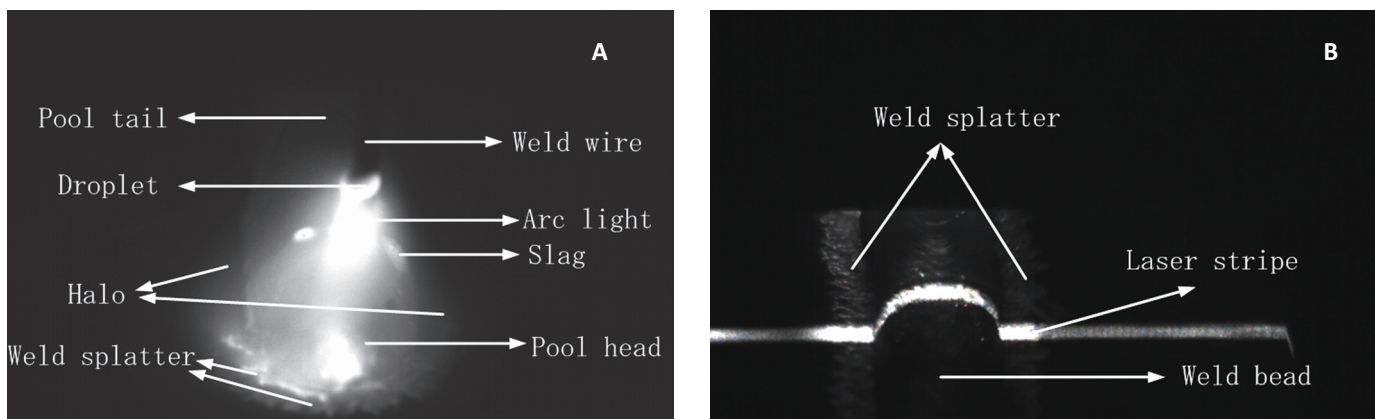


Fig. 4 — Original image: A — Weld pool; B — weld bead.

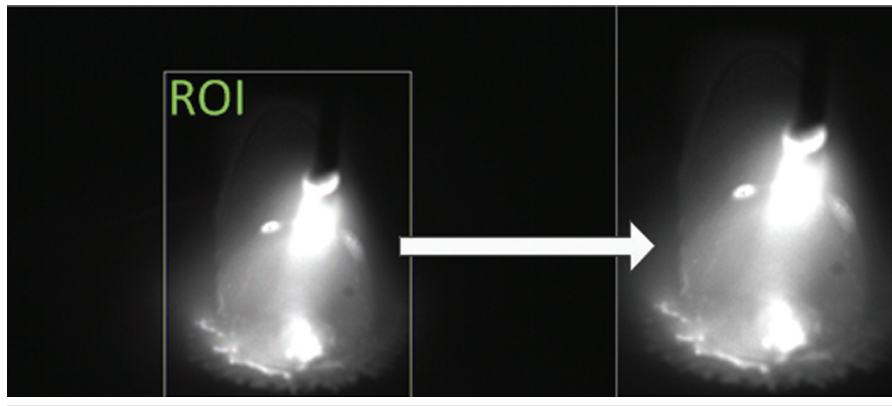


Fig. 5 — Extraction of the ROI for the weld pool image.

penetration state through a prediction model. The smaller the distance between the laser stripe and the torch, the higher the prediction accuracy of the model. In addition, considering the specular reflection of the pool and the interference of the arc light, the location parameters were identified. As the pool geometry reflects the current weld penetration state, it was also used as an input signal to revise the model parameters and improve the prediction accuracy of the model.

## Image Acquisition and Processing

A series of GMAW experiments were carried out, and the experimental conditions were listed in Table 1. Using the designed vision sensing system, the weld pool and bead images were obtained. The sample time of the system was 0.1 s. The average gray value of each image was calculated, and a threshold value was chosen to determine whether the image was shot near the base current. Figure 4 shows the

typical weld pool and weld bead images during the base current.

## Image Processing of Passive Vision

A characteristic weld pool image is presented in Fig. 4A. The image is 8-bit gray scale with a size of  $752 \times 480$  pixels. To decrease the image processing time, the region of interest (ROI) was extracted for image processing — Fig. 5. It was observed that the gray scale of the weld pool was uneven. The gray scale of the pool in the area of the arc was the strongest, and the gray scale of

the tail pool was the weakest. The gray scale of the middle area was stronger than the left and right sides because the weld pool had a spatial curved surface, and it tilted toward the front and the two sides. It made the gray scale of the weld pool area on the camera directly opposite much stronger because of the specular reflection of the arc light. As a result, the weld pool was divided into several areas: the head bright area, the tail dark area, and the middle mixed area. The length and width of the weld pool in this part will be used in future research.

## Extraction of Weld Pool Tail

An autothresholding algorithm by Otsu (Ref. 20) was applied to segment the bright area from the dark area and background. The result is shown in Fig. 6B. Figure 6C shows that the weld pool tail area is dark and located in the upper part of the image. A simple strategy was chosen to separate the weld pool tail area from the others by using the following formulas.

$$f(x,y) = \begin{cases} 1 & \text{if } I(x,y) > T \\ 0 & \text{if } I(x,y) < T \end{cases} \quad (1)$$

Table 1 — Experimental Condition of GMAW

Parameters	Values
Workpiece (Q235) dimensions (mm <sup>3</sup> )	200 × 100 × 3
Argon flow (L/min)	12
Average current (A)	100
Peak current (A)	250
Voltage (V)	24
Welding speed (mm/s)	5

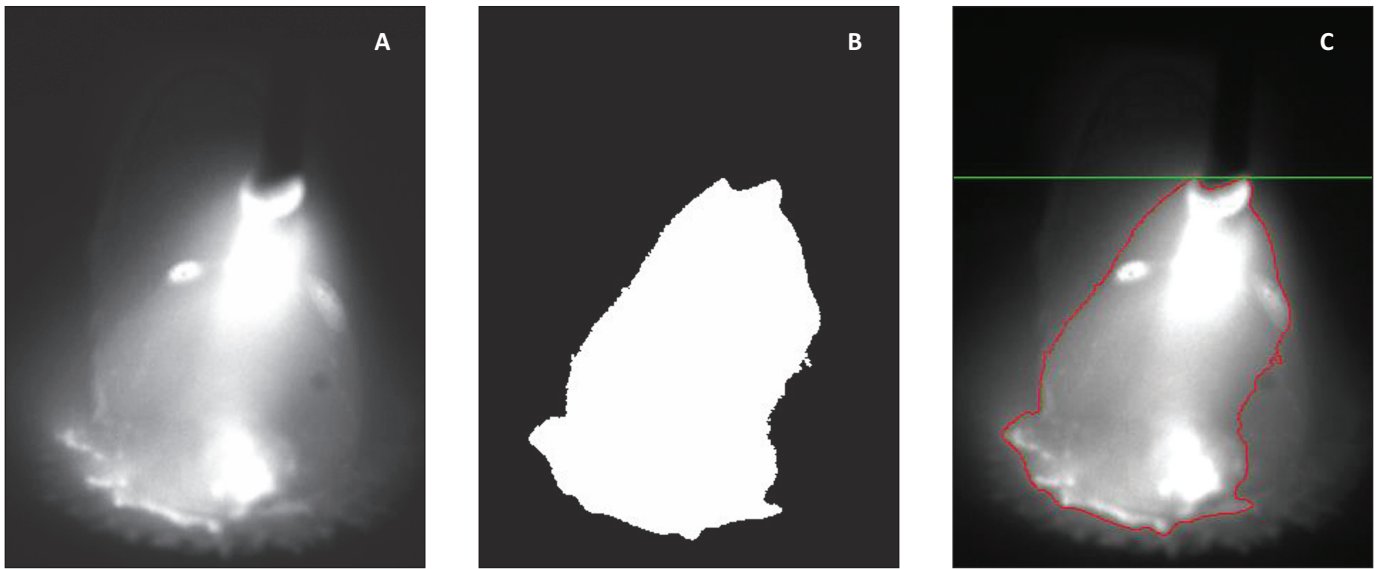


Fig. 6 — Procedure of separating the weld pool tail from the other parts: A — Original image of the weld pool; B — image after the self-adapted binary method; C — block result.

$$\text{Tailline}_Y = \max(y_i) \text{ if } f(x,y) = 1, \\ i = 1, 2, \dots n \quad (2)$$

$$\text{Parting line: } y = \text{Tailline}_Y, \\ x \in [0, \text{image.rows}] \quad (3)$$

Here,  $T$  is the autothreshold value of the weld pool image, which is self-adapting to different pool images.  $y = \text{Tailline}_Y$  is the parting line of the image to separate the weld pool tail and the other parts, which is displayed as the green line in Fig. 6C.

The gray scale change of the weld pool image at the blue line is shown in Fig. 7, in which the left edge, right edge, and the welding wire are marked in red circles.

The gray scale value of the weld pool edge was smaller than its left and right adjacent regions, which was found to be usual at the weld pool tail — Fig. 8. The cause of its formation can be summarized as two points: 1) The temperature of the weld pool edge is lower than its liquid-adjacent region. Thus, the radiation intensity of the weld pool edge was weaker than its liquid-adjacent region, and the gray scale value of the pool edge was smaller than its liquid-adjacent region. 2) The reflection of the weld pool edge was specular, and it diffused reflection in its solid-adjacent region. Thus, the reflected light of the weld pool edge that was captured by the camera was less than its solid-adjacent region, and the gray scale

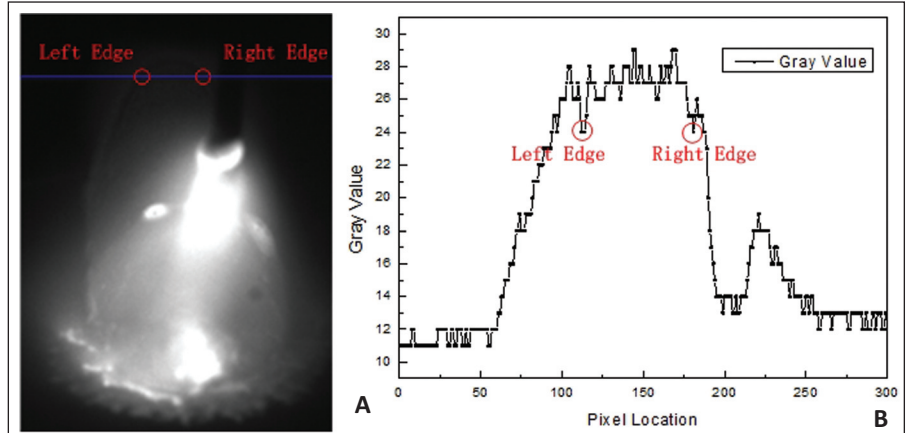


Fig. 7 — Analysis of the gray distribution for the weld pool tail: A — Original image; B — gray-level distribution at the blue line.

value of the pool edge was smaller than its solid-adjacent region.

The result shown in Fig. 7 can be easily explained through these two points. The difference of the gray scale value between the weld pool edge and its adjacent region was quite small, which caused great difficulty in extracting the edge of the weld pool tail.

The distribution of the tail gray value on the two-dimensional coordinate department is presented in Fig. 8. The position of the weld pool edge and the welding wire are also marked in this image. By observing and analyzing Figs. 7 and 8, it can be seen that the gray value of the weld pool tail edge is a little smaller than its adjacent weld pool area and weld bead area.

A threshold value  $I_1$  was calculated

by Otsu (Ref. 20), and the threshold value was used to subtract  $\Delta I$  from another threshold value, as shown in Equation 4.

$$I_2 = I_1 - \Delta I \quad (4)$$

where  $\Delta I$  is a small decrease of intensity, and 2 is selected for 256 gray levels in our case. The results of the segmentation by using the threshold value  $I_1$  and  $I_2$  are shown in Fig. 10A and B. The edges of Fig. 10A and B are extracted and shown in Fig. 10C. The plot shows that the red edge of the weld pool tail was a little farther than the red edge from the green edge. A simple strategy was proposed to extract the red edge of the weld pool tail. The position of the green pixels was searched, and the

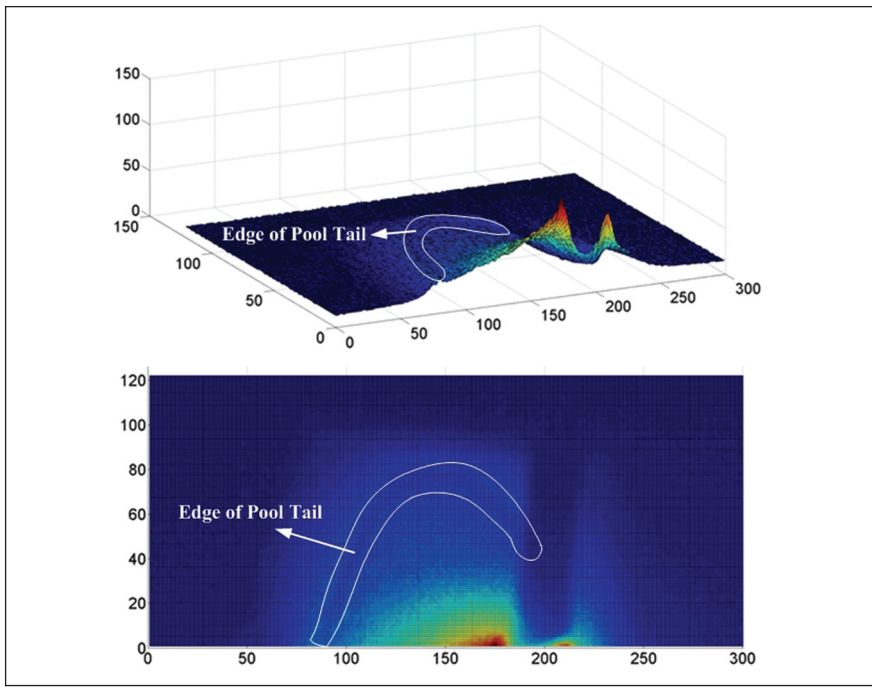


Fig. 8 — 3D gray level distribution of the weld pool tail.

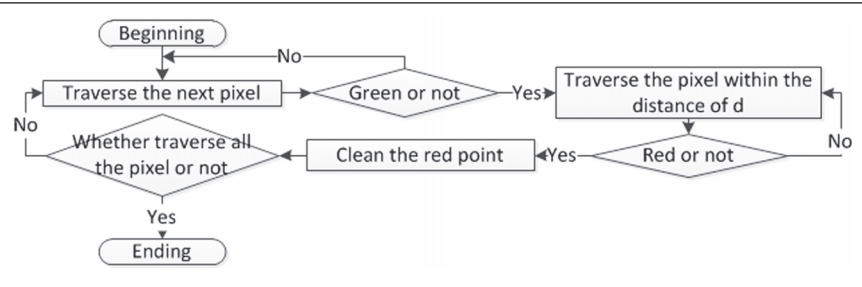


Fig. 9 — Flowchart of edge extraction for the weld pool tail.

red pixels within a certain distance threshold  $d$  from the green pixels were cleaned. The implementation process of the strategy is shown in Fig. 9.

In this paper, the distance threshold  $d$  was set to 5, and the result of the strategy was shown in Fig. 10D. A polynomial was used in our study to fit the edge of the pool tail through the red edge points in Fig. 10D, and its equation is shown as follows:

$$y = a_1 + a_2x + a_3x^2 + \dots + a_{n+1}x^n \quad (5)$$

Here,  $n = 2$  was chosen as the degree of the polynomial.  $\varepsilon_i$  was used to express the difference between the calculated  $y'$  and the actual  $y$  of the red edge points in Fig. 10D. It can be expressed as follows.

$$\varepsilon_i = y_i - (a_1 + a_2x_i + a_3x_i^2), \quad i = 0, 1, 2, 3 \dots m \quad (6)$$

The sum of the squared  $\varepsilon_i$  was used as the evaluation function of the fitting accuracy, which is shown in Equation 7. The least square method was used to determine the parameters of the polynomial equation, which made the value of function  $J$  reach the minimum. The fitting result is shown in Fig. 10E. Figure 10F shows the extracted edge of the weld pool tail in the original pool image.

$$J = \sum_{i=1}^m \varepsilon_i^2 = [y_i - (a_1 + a_2x_i + a_3x_i^2)]^2 \quad (7)$$

Finally, the position of the weld pool tail endpoint was easily calculated through the parabola obtained by fitting the edge of the weld pool tail, which is shown in Equation 8.

$$\begin{cases} x_{\text{endpoint}} = -a_2/2a_3 \\ y_{\text{endpoint}} = (4a_1a_3 - a_2^2)/4a_3 \end{cases} \quad (8)$$

### Extraction of Weld Pool Width

In this part, the width of the weld pool was extracted for future study. A regular area (the white box shown in Fig. 11A), which was treated as a small window, was selected for accurate extraction of the weld pool width. An edge-searching approach was applied to scan the image to seek for sharp gradient changes, as shown in Fig. 11B. By comparison of the result of some traditional edge detection operators that have been used in our study, the Sobel operator was found to have the best effect. A preset threshold gradient was given to detect the edge. The result is shown in Fig. 11C.

Finally, the left edge and the right edge were extracted, which is shown as the green curve in Fig. 11D. The average positions of the left and right edge in the x axis were also calculated, as seen in Equation 9.

$$\begin{cases} \text{left\_position\_x} = (\sum_{i=1}^n \text{left\_edge\_x}_i)/n \\ \text{right\_position\_x} = (\sum_{i=1}^n \text{right\_edge\_x}_i)/n \end{cases} \quad (9)$$

where  $\text{left\_edge\_x}_i$  and  $\text{right\_edge\_x}_i$  are the x values of the left and right edges. The center position of the weld pool middle can be calculated as follows.

$$x_{\text{center}} = (\text{right\_position\_x} + \text{left\_position\_x})/2 \quad (10)$$

The slope of the weld pool axis on the length direction can be calculated by the following formula:

$$\tan \theta = (y_{\text{endpoint}} - y_{\text{center}}) / (x_{\text{endpoint}} - x_{\text{center}}) \quad (11)$$

Here,  $\theta$  is the tilt angle of the weld pool axis.  $(x_{\text{endpoint}}, y_{\text{endpoint}})$  and  $(x_{\text{center}}, y_{\text{center}})$  are the position of the weld pool tail endpoint and the center position of the weld pool middle that was calculated. As a result, the weld pool width was finally expressed as the following formula.

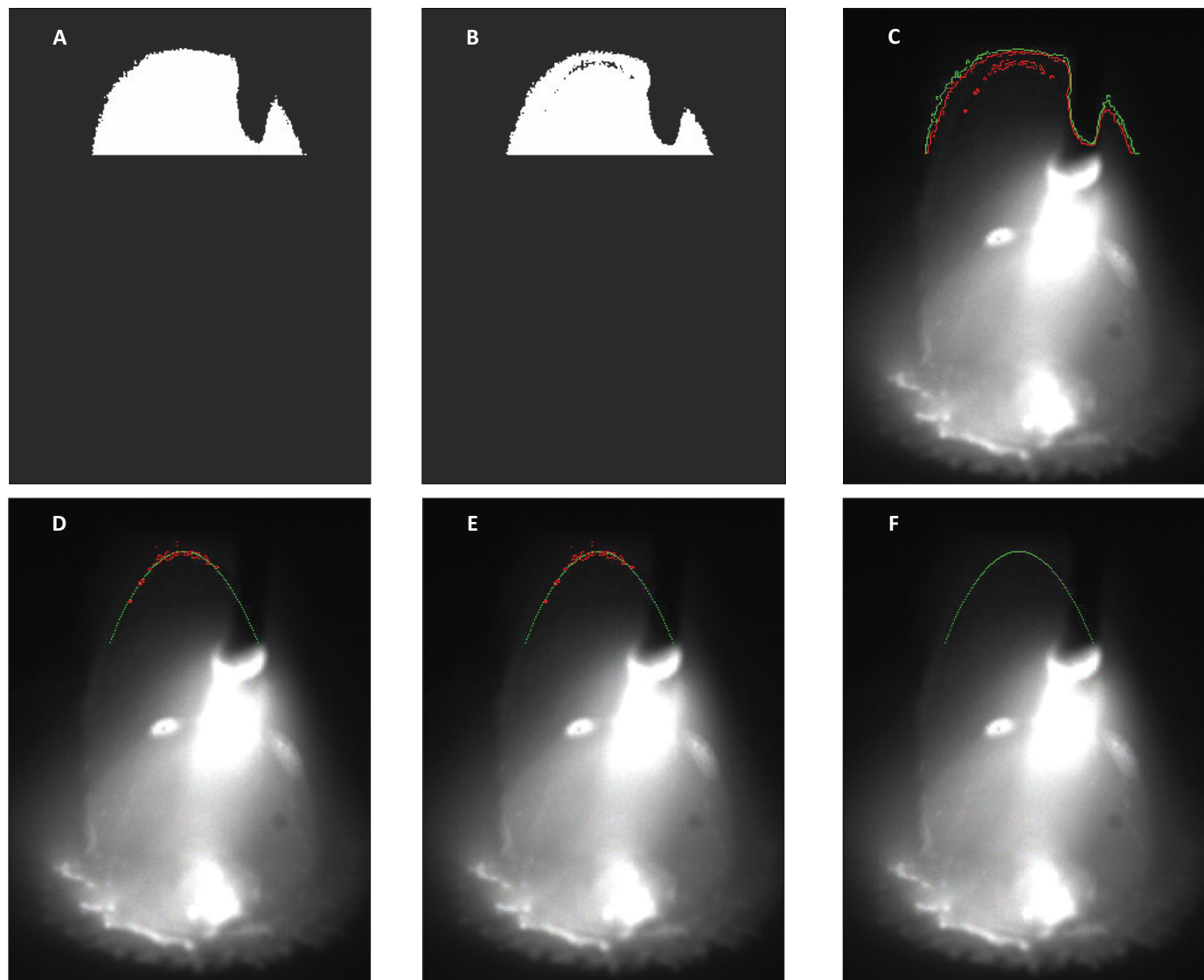


Fig. 10 — Procedure of edge extraction for the weld pool tail: A — Binary result of threshold  $I_1$ ; B — binary result of threshold  $I_2$ ; C — edge of two binary results; D — edge points of the weld pool tail; E — parabola fitting for the edge points; F — comparison of the extracted tail edge and the original image.

$$\begin{aligned} \text{Width}_{\text{pool}} &= (\text{right}_{\text{position}_x} - \text{left}_{\text{position}_x}) \\ &\quad |\sin(\pi-\theta)| \end{aligned} \quad (12)$$

#### Extraction of Weld Pool Length

In our research, the weld pool length consisted of two parts: the head length and the tail length. As shown in Fig. 12, some pool images were captured during the base current at different instants of time, and the edges of the pool heads were approximately extracted by the semicircles.

The image shows that the edge of the weld pool head had a very high approximation with the semicircle in this monitoring angle. Through the above analysis

and the observation of the weld pool shape, the geometrical characteristic of the weld pool can be illustrated by Fig. 13, where the feature of the weld pool can be represented by the head length, tail length, and the width.

As the weld pool head was approximated by a semicircle, the head length was also expressed by the weld pool width, as shown in Equation 13. The tail length and width of the weld pool were extracted as the features to be controlled in our research.

$$\text{Length}_{\text{poolhead}} = \text{Width}_{\text{pool}}/2 \quad (13)$$

As shown in Fig. 6B, the bright area is segmented from the dark area and background by an autothresholding al-

gorithm. The edge of the bright area is shown as the red curve in Fig. 14.

The yellow line represents the axis of the weld pool on the length direction. The intersection points of the pool axis and the red curve were calculated, and the intersection point near the weld pool head was its endpoint.

$$\begin{aligned} \text{Length}_{\text{pooltail}} &= \frac{y_{\text{endpoint}} - y_{\text{headpoint}}}{|\sin(-\pi\theta)|} \\ &= \text{Length}_{\text{poolhead}} \end{aligned} \quad (14)$$

#### Image Processing of Active Vision

Figure 15 displays the most popular

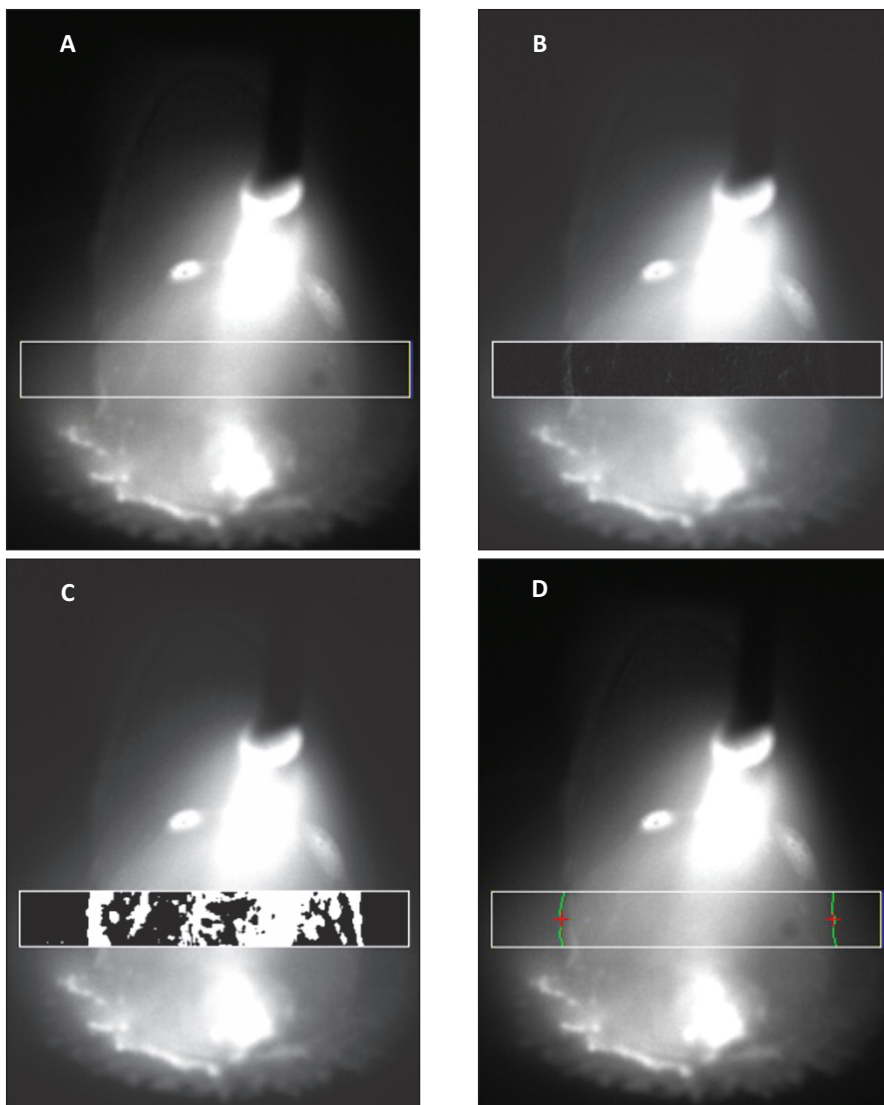


Fig. 11 — Procedure of left and right edge extraction for pool middle: A — Original image; B — Sobel operator; C — adapted binary; D — extraction of the left and right edge.

image of the weld bead and the laser stripe that was captured by the active vision system. As analyzed from the bead image, a ROI was defined first. Considering the resolution of the captured image and the position of the laser stripe in the image, we defined the ROI as shown in Fig. 15.

The traditional edge detection operator Sobel (Ref. 21) was implemented to detect the edge of the laser stripe where the gradient of the image gray scale had drastic change. The result is shown in Fig. 16A. The lower boundary of the laser stripe is extracted by the following equations, and the extraction result is shown in Fig. 16B.

$$T_i = \max(G_{ij}) - \Delta g, i = 1, 2, 3, \dots, m; j = 1, 2, 3, \dots, n \quad (15)$$

$$y'_i = \min(y_{ij}) \text{ if } G_{ij} > T_i, \\ i = 1, 2, 3, \dots, m; j = 1, 2, 3, \dots, n \quad (16)$$

where  $T_i$  is the threshold for the gradient in column  $i$ , and  $G_{ij}$  is the gradient value in  $(i, j)$ . The  $\Delta g$  was a decrease of intensity, and 30 was selected in our application.  $y'_i$  was the ordinate of the laser stripe's lower boundary in column  $i$ , and  $y_{ij}$  was the ordinate of the point  $G_{ij} > T_i$ .

As shown in Fig. 16B, the extracted lower boundary of the laser stripe was not smooth enough, and there were still some abnormal points that made the curve discontinuous. A simple strategy was used to solve this problem. The ordinate of the boundary point  $y''_i$  was calculated by the average

of its left and right adjacent boundary points. The computational method is shown in Equation 17, and the result is shown in Fig. 16C. Figure 16D shows a comparison between the extracted lower boundary of the laser stripe and the original image.

$$y''_i = (\sum_{j=-3}^3 y'_{i+j} - y'_i)/6 \quad (17)$$

The boundary points of the bead that was marked as the green crosses were extracted by seeking the positions of the sharp gradient changes in the curve — Fig. 17.

The highest position of the bead was also easily found and marked as the green line by seeking the highest point in the curve. The feature of the weld bead (height and width) was calculated with the following equations:

$$\text{Height}_{\text{bead}} = y_{\text{line}} - (y_{\text{left}} + y_{\text{right}})/2 \quad (18)$$

$$\text{Width}_{\text{bead}} = x_{\text{right}} - x_{\text{left}} \quad (19)$$

Here,  $y_{\text{line}}$  is the coordinate of the highest point in the curve.  $(x_{\text{left}}, y_{\text{left}})$  and  $(x_{\text{right}}, y_{\text{right}})$  are the coordinates of the left and right boundary points of the weld bead.

## Precision Verification

To verify the validity of the above image processing algorithm, extra experiments were conducted. The manual and detected values were compared, and the mean square errors were calculated as the criterion to evaluate the precision of the passive vision algorithm and the active vision algorithm through a series of images that were obtained by the vision system. Figure 18A and B show the comparison of the manual and detected values for the pool width and length, respectively. The mean square errors of the weld pool width and length were 20.88 and 27.07, respectively. The manual and detected values for the weld bead width and height are presented in Fig. 19A and B, respectively. The mean square errors of the pool width and length were 10.17 and 6.39, respectively.

## Conclusion

A monitoring system including pas-

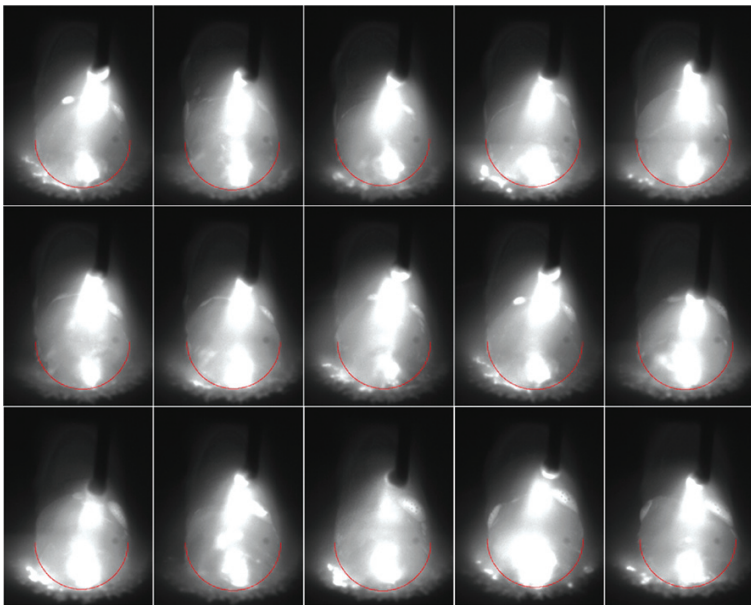


Fig. 12 — Analysis of the feasibility to approximate the pool head with semicircles.

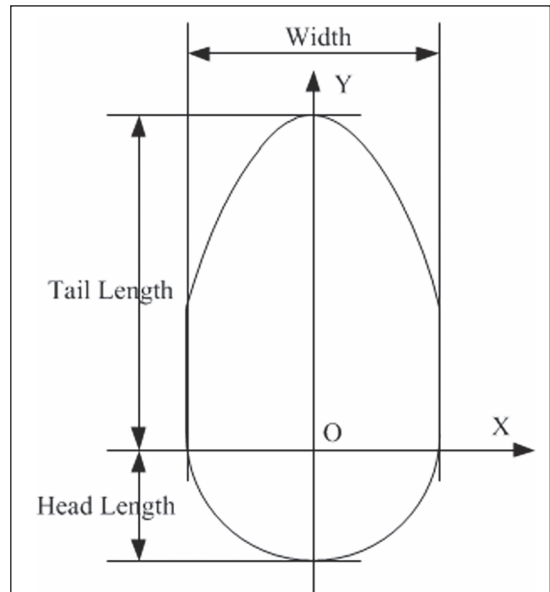


Fig. 13 — Weld pool characteristic parameters.



Fig. 14 — Extraction of the pool head endpoint.

sive vision and active vision has been developed for weld pool and weld bead geometry measurement in GMAW. The passive vision part was for pool detection, and the active vision part was for weld bead detection.

Through the careful analysis of the pool image gray scale, the pool feature was separated into three parts to be extracted: the pool tail, the pool middle, and the pool head. The dynamic

bithreshold method was proposed, and the points of the tail edge were obtained through this method. By observing the geometrical shape of the weld pool tail, the edge of the pool tail was extracted through the fitting of a parabola using the least-square method.

A semicircle was used to approximate the weld pool head after observing a series of pool images. The width of the weld pool was obtained through the extraction of the left and right edges of the pool middle. The weld pool axis was also calculated through the vertex of the fitting parabola and the center position of the weld pool middle. The intersection of the weld pool axis and the edge of the weld pool head were calculated as the endpoint of the weld pool head. The tail length of the weld pool was finally obtained.

In the active vision part, the Sobel edge detection was applied, and the

lower edge of the laser stripe was extracted by seeking the lowest edge on the basis of setting a threshold value for the result of the Sobel edge detection. A smooth algorithm was proposed to remove the distortional point. The boundary points of the bead were extracted by seeking the positions of the sharp gradient changes in the curve, and the top of the bead was also extracted by the maximum of the curve. The width and the height of the weld bead were finally calculated through the boundary points and the top position of the bead.

Under the condition of our existing hardware, the image processing algorithms of active and passive vision took 19.13 and 51.66 ms, respectively. This speed of image processing is enough to meet the real-time demands of the system.

The verification test was finally conducted, and that showed the proposed image processing algorithm was reli-

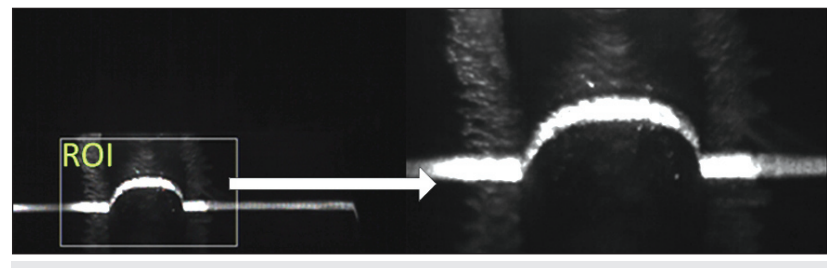


Fig. 15 — Extraction of the ROI for the weld bead image.

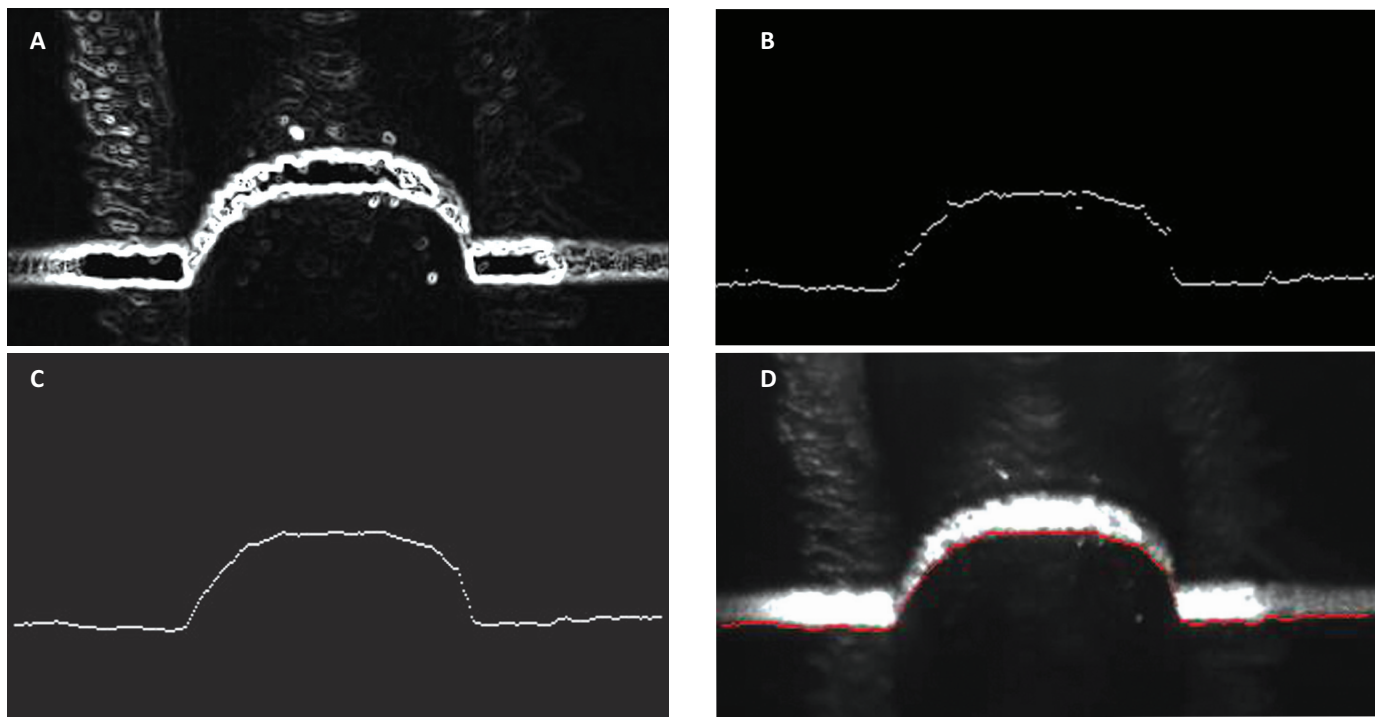


Fig. 16 — Procedure of lower edge extraction for laser stripe: A — Sobel operator; B — extraction result; C — smooth result; D — comparison of the extracted curve and the original image.

able, and that detection precision can meet the requirement of the GMAW process.

Control of the GMAW process was the aim of this study. Future work will include the following: 1) Establishing the relationship between the backside melting width and the feature of the weld pool and weld bead; and 2) establishing a closed-loop control system for the GMAW process.

## References

1. Wang, Z. Z. 2016. A laser back-lighting based metal transfer monitoring system for robotic gas metal arc welding. *Robotics and Computer-Integrated Manufacturing* 38: 52–66.
2. Cruz, J. G., Torres, E. M., and Alfaro, S. C. A. 2015. A methodology for modeling and control of weld bead width in the GMAW process. *Journal of the Brazilian Society of Mechanical Sciences and Engineering* 37(5): 1529–1541.
3. Lv, N., Zhong, J. Y., Chen, H. B., Lin, T., and Chen, S. B. 2014. Real-time control of welding penetration during robotic GTAW dynamical process by audio sensing of arc length. *International Journal of Advanced Manufacturing Technology* 74: 235–249.
4. Liu, Y. K., Zhang, W. J., and Zhang, Y. M. 2013. Dynamic Neuro-fuzzy Estimation of the Weld Penetration in GTAW Process. *IEEE International Instrumentation and Measurement Technology Conference* 80(11): 1380–1385.
5. Mi, B., and Ume, C. 2006. Real-time weld penetration depth monitoring with laser ultrasonic sensing system. *Journal of Manufacturing Science and Engineering* 128(1): 280–286.
6. Fan, H., Ravalal, N. K., Wikle, H. C., and Chin, B. A. 2003. Low-cost infrared sensing system for monitoring the welding process in the presence of plate inclination angle. *Journal of Materials Processing Technology* 140: 668–675.
7. Guu, A. C., and Rokhlin, S. I. 1989. Computerized radiographic weld penetration control with feedback on weld pool depression. *Materials Evaluation* 47(10): 1204–1210.
8. Zhang, Y. M., Wu, L., Walcott, B. L., and Chen, D. H. 1993. Determining joint penetration in GTAW with vision sensing of weld-face geometry. *Welding Journal* 72(10): 463-s to 469-s.
9. Zhang, Y. M., Kovacevic, R., and Li, L. 1996. Adaptive control of full penetration GTA welding. *IEEE Transactions on Control Systems Technology* 4(4): 394–403.
10. Zhang, Y. M., and Kovacevic, R. 1998. Neurofuzzy model-based predictive control of weld fusion zone geometry. *IEEE Transactions on Fuzzy Systems* 6(3): 389–401.
11. Zhang, Y. M., and Kovacevic, R. 1997. Real-time image processing for monitoring of free weld pool surface. *Journal of Manufacturing Science and Engineering* 119(2): 161–169.
12. Zhao, C. X., Richardson, I. M., Kenjeres, S., Kleijn, C. R., and Saldi, Z. 2009. A stereo vision method for tracking particle

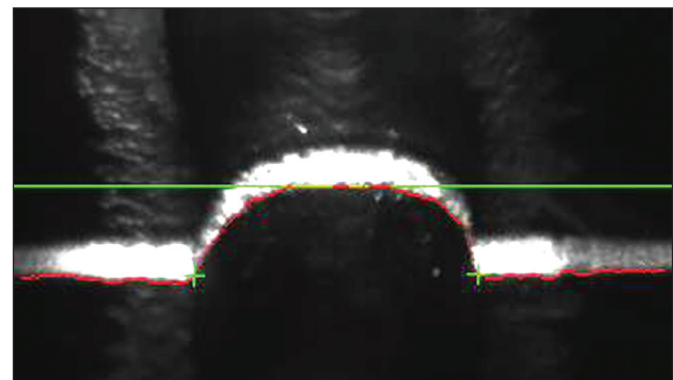


Fig. 17 — Extraction of the boundary points and the top position of the weld bead.

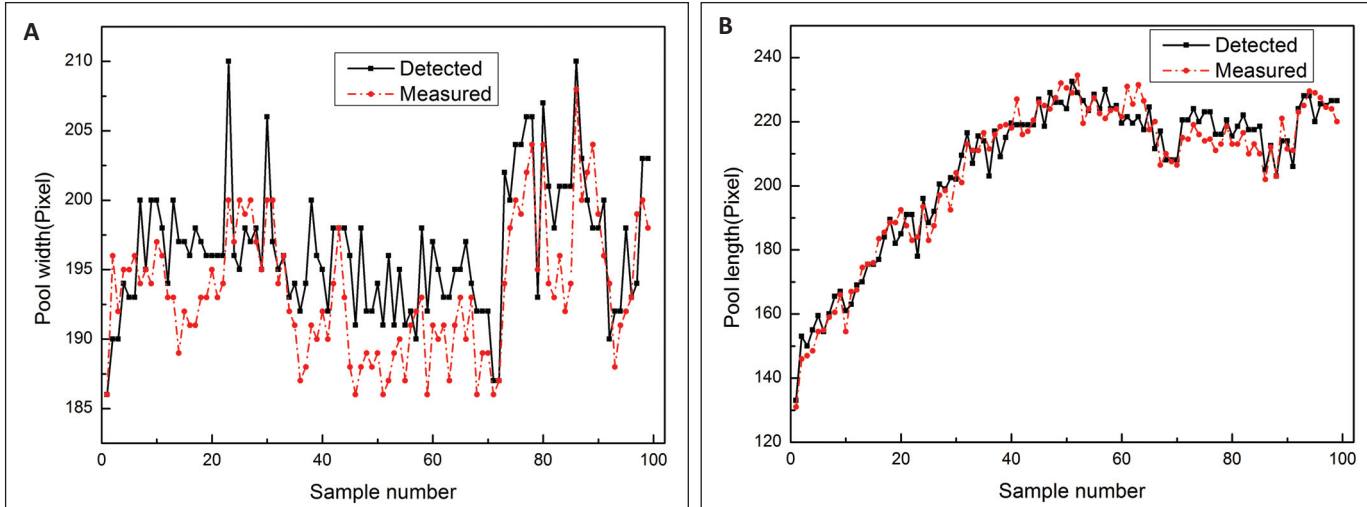


Fig. 18 — Comparison of manual and detected values: A — Pool width; B — pool length.

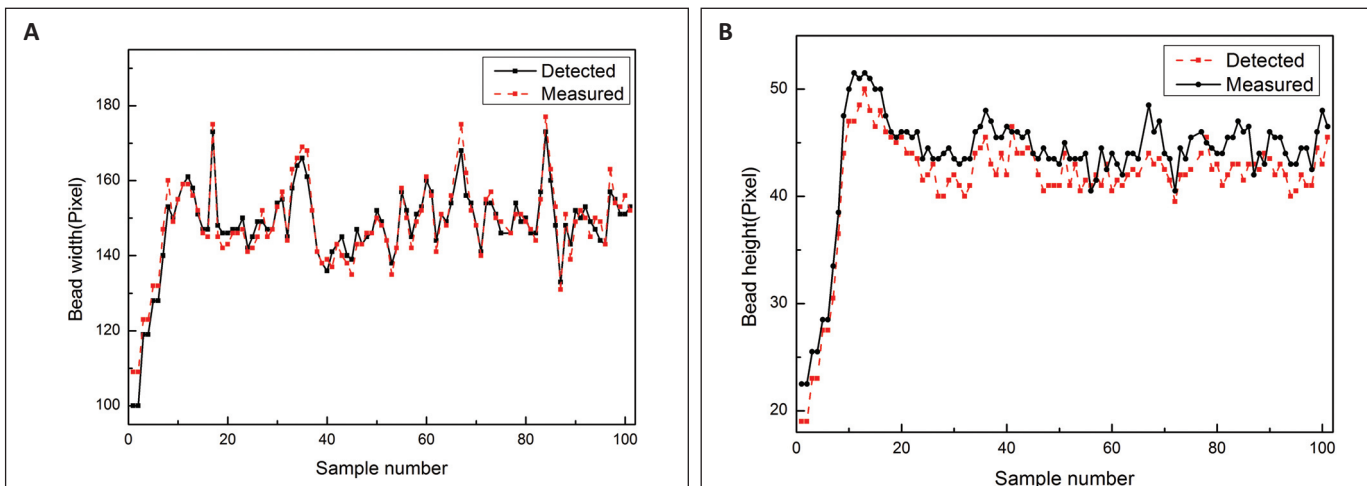


Fig. 19 — Comparison of manual and detected values: A — Bead width; B — bead height.

flow on the weld pool surface. *Journal of Applied Physics* 105 (123104): 1–8.

13. Ma, H. B., Wei, S. C., Lin, T., Chen, S. B., and Li, L. P. 2010. Binocular vision system for both weld pool and root gap in robot welding process. *Sensor Review* 30(2): 116–123.

14. Fan, C. J., Lv, F. L., and Chen, S. B. 2009. Visual sensing and penetration control in aluminum alloy pulsed GTAW welding. *International Journal of Advanced Manufacturing Technology* 42(1): 126–137.

15. Zhang, Y. M., Song, H. S., and Saeed, G. 2006. Observation of a dynamic specular weld pool surface. *Measurement*

*Science and Technology* 17(6): L9–L12.

16. Song, H. S., and Zhang, Y. M. 2007. Three-dimensional reconstruction of specular surface for gas tungsten arc weld pool. *Measurement Science and Technology* 18(12): 3751–3767.

17. Zhang, W. J., Liu, Y. K., and Zhang, Y. M. 2013. Real-time measurement of the weld pool surface in GTAW process. *IEEE International Instrumentation and Measurement Technology Conference* 80(11): 1640–1645.

18. Aviles-Vinas, J. F., Rios-Cabrera, R., and Lopez-Juarez, I. 2016. On-line learning of welding bead geometry in industrial

robots. *International Journal of Advanced Manufacturing Technology* 83: 217–231.

19. Aviles-Vinas, J. F., Lopez-Juarez, I., and Rios-Cabrera, R. 2015. Acquisition of welding skills in industrial robots. *Industrial Robot* 42(2): 156–166.

20. Otsu, N. 1979. A threshold selection method from gray-level histograms. *IEEE Transactions on Systems Man and Cybernetics* 9(1): 62–66.

21. Marr, D., and Hildreth, E. 1980. Theory of edge detection. *Proceedings of the Royal Society of London* 207: 187–217.

ZESHI JIN, HAICHAO LI (lihaichao@hit.edu.cn), QIYUE WANG, and HONGMING GAO are with the State Key Laboratory of Advanced Welding and Joining, Harbin Institute of Technology, China.